




**Broken  $C_4$  symmetry in the tetragonal state of uniaxial strained  $\text{BaCo}_{0.9}\text{Ni}_{0.1}\text{S}_{1.9}$** Shin-ichi Shamoto <sup>1,2,3,4,\*</sup>, Hiroki Yamauchi,<sup>5</sup> Kazuhiko Ikeuchi,<sup>1</sup> Ryoichi Kajimoto <sup>6</sup>, and Jun'ichi Ieda <sup>3</sup><sup>1</sup>Neutron Science and Technology Center, Comprehensive Research Organization for Science and Society (CROSS), Tokai, Ibaraki 319-1106, Japan<sup>2</sup>Department of Physics, National Cheng Kung University, Tainan 70101, Taiwan<sup>3</sup>Advanced Science Research Center, Japan Atomic Energy Agency (JAEA), Tokai, Ibaraki 319-1195, Japan<sup>4</sup>Meson Science Laboratory, RIKEN, Wako, Saitama 351-0198, Japan<sup>5</sup>Materials Sciences Research Center, Japan Atomic Energy Agency (JAEA), Tokai, Ibaraki 319-1195, Japan<sup>6</sup>J-PARC Center, Japan Atomic Energy Agency (JAEA), Tokai, Ibaraki 319-1195, Japan

(Received 16 October 2020; revised 21 December 2020; accepted 16 January 2021; published 22 February 2021)

A compound with large anions is known to show large compressibility, whereby a novel response may emerge from the degenerated state by a uniaxial pressure. Neutron scattering study of  $\text{BaCo}_{0.9}\text{Ni}_{0.1}\text{S}_{1.9}$  crystal reveals that the tetragonal insulating state has two magnetic domains with in-plane anisotropic antiferromagnetic wave vectors  $\mathbf{Q}_1 = (\pi, 0)$  and  $\mathbf{Q}_2 = (0, \pi)$ . The magnetic order with in-plane broken  $C_4$  symmetry is realized as a twin of these two domains in the tetragonal state without any strain. One magnetic domain with  $\mathbf{Q}_2$  becomes dominant under a weak strain without any appreciable structural distortion. Correspondingly, the in-plane broken  $C_4$  symmetry is also observed in the in-plane magnetic excitation of the tetragonal state.

DOI: [10.1103/PhysRevResearch.3.013169](https://doi.org/10.1103/PhysRevResearch.3.013169)**I. INTRODUCTION**

Broken symmetries are sometimes hindered in a high-symmetry state due to degeneracy. Such a state inevitably accompanies with strong fluctuations, leading to intrinsic novel properties different from the others. In the antiferromagnetic (AF) stripe order on a two-dimensional layer, there can exist two AF wave vectors  $\mathbf{Q}_1 = (\pi, 0)$  and  $\mathbf{Q}_2 = (0, \pi)$ , as shown in Figs. 1(a) and 1(b), respectively [1]. In the case of spins parallel to the  $a$ -axis, the former is that the spins align normal to the ferromagnetic chain with AF wave vector of  $\mathbf{Q}_1$ , which is observed in iron-based superconductor parent compounds [2,3] [Fig. 1(a)]. The latter is that the spins align parallel to the ferromagnetic chain with AF wave vector of  $\mathbf{Q}_2$ . These in-plane anisotropic spin structures are intensively discussed in the context of spin nematicity in a paramagnetic state of iron-based superconductors [1]. In addition, the two-dimensional (2D) layer with the nearest-neighbor ferromagnetic interaction and the second-nearest neighbor antiferromagnetic interaction can be regarded as 2D version of a frustrated  $J_1$  and  $J_2$  magnetic chain, where multipolar spin correlation may play an important role [4]. The discussions in a 2D magnetic system, however, are so far limited in iron pnictides [3] and the family compound  $\text{KFe}_{0.8}\text{Ag}_{1.2}\text{Te}_2$  [5,6]. The stripe order has been studied theoretically [2,7,8] where a theoretical phase diagram of isotropic  $J_1 - J_2$  model shows rich

phases such as nematic quantum spin liquid next to the stripe order [7]. Based on the inelastic neutron scattering (INS) measurement of  $\text{CaFe}_2\text{As}_2$  [9], the in-plane first-nearest-neighbor exchange coupling parameters  $SJ_{1a} = 49.9$  meV and  $SJ_{1b} = -5.7$  meV are strongly anisotropic in the orthorhombic state weakly distorted from a tetragonal lattice. The strong anisotropy is attributed to the degeneracy lifting of Fe  $3d_{yz}$  and  $3d_{zx}$  orbitals below the tetragonal-to-orthorhombic phase transition. The in-plane broken  $C_4$  symmetry is apparently hindered due to the equally distributed twin domains in the tetragonal state, where the magnetic domains are supposed to be inherently fluctuating [10]. When the tetragonal state is weakly distorted to an orthorhombic state by a uniaxial pressure, the lattice distortion leads to a manifestation of one magnetic domain [11–13]. Such a domain change is observed in  $\text{BaFe}_2\text{As}_2$  under a uniaxial pressure of  $\sim 0.7$  MPa along the  $b$ -axis [10]. It has also been observed in the inelastic neutron scattering pattern as the intensity difference between  $(1, 0)$  and  $(0, 1)$  in the  $(H, K)$  plane [12], where the in-plane anisotropy has been confirmed even in the tetragonal metallic state under a uniaxial pressure.

Here, we focus how the  $C_4$  symmetry is broken in this tetragonal insulating state of  $\text{BaCo}_{1-x}\text{Ni}_x\text{S}_{2-y}$  with a two-dimensional layered structure [14] as another novel interesting platform where the AF stripe order emerges. All magnetic ordered states studied previously are in orthorhombic state [3,5,6]. Contrasted to these previous compounds, the present material exhibits the AF stripe order in the tetragonal state. In addition, this class exhibits a metal-insulator (MI) transition [15,16] as two-dimensional Mott transition with multi-orbital state [14,17]. Especially,  $x = y = 0.1$ , i.e.,  $\text{BaCo}_{0.9}\text{Ni}_{0.1}\text{S}_{1.9}$  (BCNS) exhibits MI transition with increasing temperature from a paramagnetic metal (PM) to an AF insulator (AFI) [15,18–20] accompanied by a structural phase

\*s\_shamoto@cross.or.jp

Published by the American Physical Society under the terms of the [Creative Commons Attribution 4.0 International license](https://creativecommons.org/licenses/by/4.0/). Further distribution of this work must maintain attribution to the author(s) and the published article's title, journal citation, and DOI.

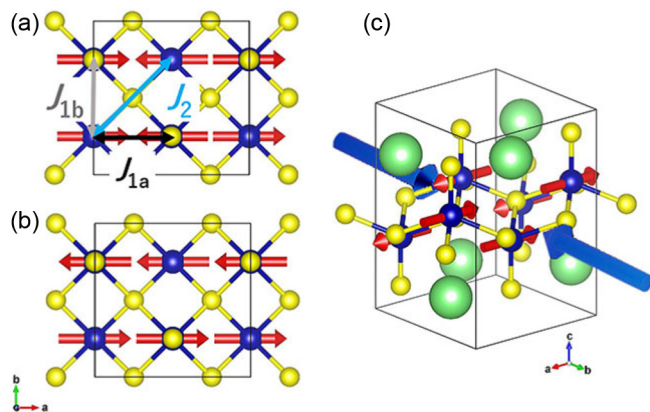


FIG. 1. Two types of stripe order structures in a two-dimensional  $\text{Co}_{0.9}\text{Ni}_{0.1}\text{S}_{1.9}$  layer and magnetic exchange couplings. (a)  $\mathbf{Q}_1 = (\pi, 0)$  observed in iron-based superconductor parent materials. The magnetic moments (red arrows) align along the  $a$ -axis with the AF wave vector of  $\mathbf{Q}_1$  in the two-dimensional square lattice. Three exchange coupling parameters,  $J_{1a}$ ,  $J_{1b}$ , and  $J_2$  are major parts for the spin-wave calculation. (b)  $\mathbf{Q}_2 = (0, \pi)$ . The magnetic moments align along the  $a$ -axis with the AF wave vector of  $\mathbf{Q}_2$ . (c) Three-dimensional view of the magnetic structure in panel (b).  $\text{Co}_{0.9}\text{Ni}_{0.1}$  (blue) is coordinated by a pyramid of five sulfur ions (yellow).  $\text{Co}_{0.9}\text{Ni}_{0.1}$  ions alternately buckle along the  $c$ -axis in the layer due to the alternating buckling of apical sulfur ions. Uniaxial pressure is applied along  $b$  axis. The exchange coupling parameter  $SJ_c$  is between two Fe magnetic moments at equivalent sites in the neighboring unit cells along  $c$  axis.

transition. The PM phase disappears at a uniform pressure of 280 MPa [18] associated with the large compressibility owing to large anion (sulfur) atoms. The AF ordering takes place at Néel temperature of 280 K above the tetragonal-to-orthorhombic phase transition temperature ( $T_s$ ) at 185–235 K that enables us to disentangle the magnetic domain change and the structural transition, although its detailed spin configuration has not been determined to be either  $\mathbf{Q}_1$  or  $\mathbf{Q}_2$  because of the degeneracy in the tetragonal  $C_4$  symmetry. In this work, we report that the  $\mathbf{Q}_2$  domain out of coexisting  $\mathbf{Q}_1$  and  $\mathbf{Q}_2$  domains becomes dominant by applying a weak in-plane uniaxial pressure of 1 MPa in the AFI phase of BCNS. Our inelastic neutron scattering (INS) measurements of the crystal at a weak uniaxial pressure of 1 MPa reveals a characteristic in-plane anisotropy of magnetic excitation in the tetragonal state. The magnetic excitation spectra are distinct from those observed in detwinned  $\text{BaFe}_{2-x}\text{Ni}_x\text{As}_2$  crystals at uniaxial pressures [11,12]. The spectra of BCNS in the insulator phase are described by a spin-wave model with  $\mathbf{Q}_1$  and  $\mathbf{Q}_2$  domains, leading to the estimation of the exchange couplings. Thus, it provides us quantitative information on the magnetic excitation stabilizing the novel stripe order in the tetragonal state. The three-dimensional view of the determined magnetic structure for the major  $\mathbf{Q}_2$  domain is shown in Fig. 1(c).

## II. EXPERIMENTAL PROCEDURES

Single crystals of  $\text{BaCo}_{0.9}\text{Ni}_{0.1}\text{S}_2$  have been successfully grown by the Bridgman method [21]. After cutting out

single crystals from an ingot, they were annealed at 1173 K in a vacuum with a small amount of Zr metal in a sealed quartz tube. The sulfur deficiency was determined as  $y = 0.12$  in  $\text{BaCo}_{0.9}\text{Ni}_{0.1}\text{S}_{2-y}$  from the weight loss after the annealing.

Neutron scattering measurements of a BCNS crystal with a weight of 0.75 g were carried out at uniaxial pressures using the chopper spectrometer 4SEASONS [22] with a multi- $E_i$  option [23] in J-PARC with a proton beam power of 500 kW. The magnetic tetragonal unit cell with four Co(Ni) atoms have lattice parameters of  $a = b = 6.43 \text{ \AA}$  and  $c = 8.91 \text{ \AA}$  at 200 K.

In the elastic neutron scattering measurement, the crystal was rotated by  $1^\circ$  step from  $-38^\circ$  to  $42^\circ$  in the scattering plane of [100] and [001]. It took 70 s per each scan, resulting in about 2 h in total. In the analysis, the measured intensity was integrated in the four-dimensional space of  $|H - Q_a| \leq 0.2 \text{ r.l.u.}$ ,  $|K - Q_b| \leq 0.2 \text{ r.l.u.}$ ,  $|L - Q_c| \leq 0.2 \text{ r.l.u.}$ ,  $|E| \leq 10 \text{ meV}$ . The uniaxial pressures were applied along the  $b$ -axis by using a mechanical spring with  $P = 0.1$  and 1 MPa. The ingot crystal was fragile, limiting the pressure value to 1 MPa. The neutron Laue diffraction shows an in-plane mosaic spread of  $1.92 \pm 0.06$  degrees. In a tetragonal phase,  $a$  and  $b$  axes are equivalent to each other. However, the spin direction was uniquely determined to be preferentially along the  $a$ -axis normal to the uniaxial pressure direction in our magnetic structure analysis by FULLPROF software [24]. The nuclear and magnetic structures in Fig. 1 were generated by VESTA [25]. Note that the tetragonal phase did not show any orthorhombic distortion at the present weak uniaxial pressure within our experimental accuracy.

In the inelastic neutron scattering measurement, the  $c$ -axis of the crystal was set to be parallel to the incident beam direction. In this setting,  $L$  in the reciprocal space of  $(H, K, L)$  changes from 0.7 to 3.4 r.l.u. with increasing the transfer energy ( $E$ ) from 40 to 80 meV for  $E_i = 120.0 \text{ meV}$ , whereas  $L$  increases from 1.6 to 3.7 r.l.u. with increasing  $E$  from 10 to 30 meV for  $E_i = 54.1 \text{ meV}$ . The index of the reciprocal space is expressed only by the in-plane index  $(H, K)$ , because of the high two-dimensionality of BCNS.  $H$ ,  $K$ , and  $L$  are in reciprocal lattice units (r.l.u.). The data were analyzed by using UTSUSEMI software [26]. Observed dynamical structure factors were estimated on an absolute scale ( $\text{mbarn sr}^{-1} \text{ meV}^{-1} \text{ Co}^{-1}$ ) by comparing the count rate with that from a plate of vanadium. The detector efficiency depending on  $E_f$  was also corrected. The imaginary part of the dynamical spin susceptibility was obtained by an equation for isotropic paramagnet [27] including the Bose factor and the isotropic magnetic form factor for  $\text{Co}^{2+}$ . Doped Ni was neglected for INS measurements because of the similarity of Ni to Co in addition to the small concentration of Ni. The spin excitations were calculated by SPINW software [28] with a set of exchange coupling parameters, which are the anisotropic first-nearest-neighbor ferromagnetic interactions  $SJ_{1a}$ ,  $SJ_{1b}$ , the second-nearest-neighbor AF interaction  $SJ_2$ , and the ferromagnetic out-of-plane interaction  $SJ_c$ , based on the observed magnetic structure. The calculation is based on the linear spin-wave theory with the Holstein-Primakoff approximation. The calculated scattering patterns were drawn by HORACE software [29].

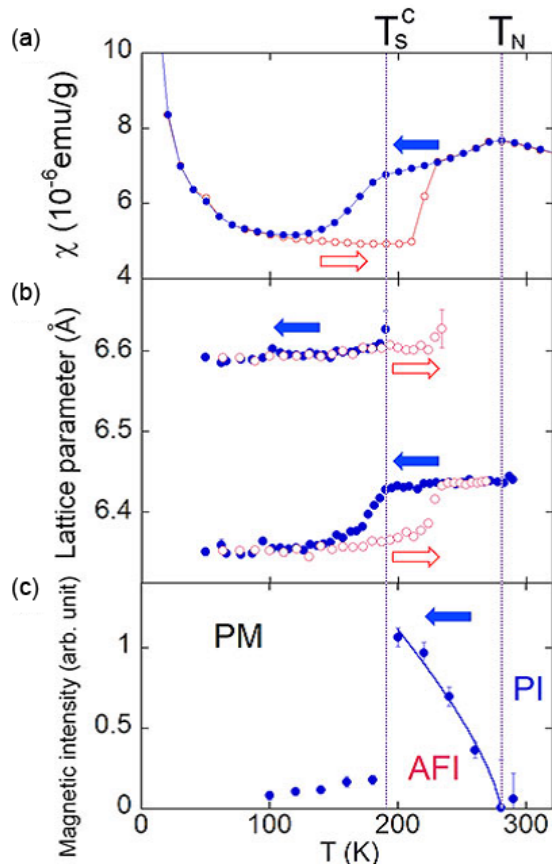


FIG. 2. Temperature dependence of magnetic susceptibility, in-plane lattice parameters, and magnetic peak intensity. (a) Temperature dependencies of the field-cooled and zero-field-cooled DC magnetic susceptibilities ( $\chi = M/B$ ) curves at an ambient pressure. The peak appears at the Néel temperature  $T_N$ . A hysteresis is observed in the mid-temperature range. (b) In-plane lattice parameters estimated from 400 and 040 peaks at a uniaxial pressure of 1 MPa along the  $b$ -axis. The tetragonal-to-orthorhombic phase transition  $T_S$  can be observed by the splitting of the peaks. Filled circles and open circles denote cooling and warming processes, respectively. (c) Temperature dependence of 102 magnetic Bragg peak intensity obtained by the neutron diffraction measurement upon cooling at a uniaxial pressure of 1 MPa along the  $b$ -axis. Below the structural phase transition  $T_S^c$  upon cooling, the intensity suddenly drops. The solid line is a guide to the eye. The arrows denote the thermal cycle directions. PM, AFI, and PI are the paramagnetic metal phase, antiferromagnetic insulator phase, and paramagnetic insulator phase, respectively.

### III. RESULTS

#### A. Phase transitions and magnetic structures

Figures 2(a)–2(c) show the temperature dependence of the physical properties of a single crystal BCNS. The magnetic susceptibility is accompanied by the sharp increase at the first-order phase transition from PM to AFI phases [Fig. 2(a)]. The transitions take place at 187 K upon cooling and 220 K upon warming, accompanied by the orthorhombic-to-tetragonal phase transition [Fig. 2(b)]. The temperature dependence of a 102 magnetic Bragg peak [Fig. 2(c)] shows a Néel temperature of 280 K, which does not shift by the

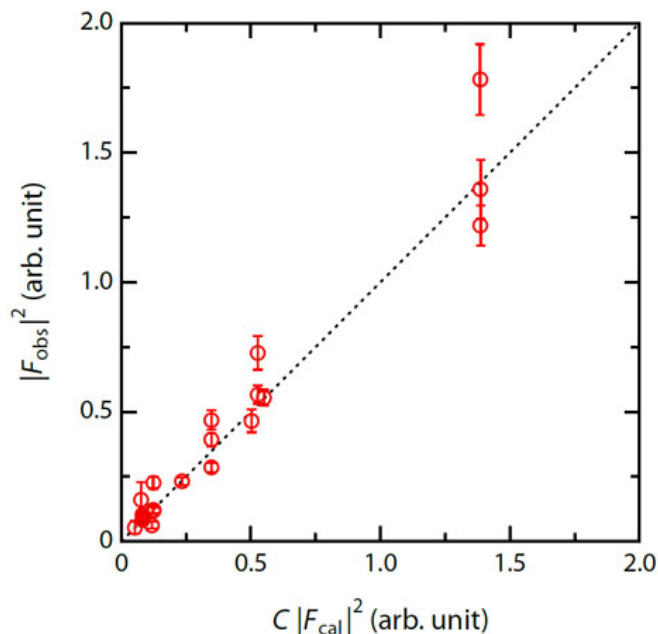


FIG. 3. Observed nuclear Bragg peak intensities as a function of calculated intensity. The measurement of BCNS crystal was carried out at a uniaxial pressure of 1 MPa.

uniaxial pressure in the magnetic susceptibility measurement of Fig. 2(a). The magnetic excitation at the uniaxial pressure was measured by INS in the tetragonal AFI phase at 200 K upon cooling well above the structural phase transition at 187 K. In the PM phase at low temperatures, the magnetic Bragg peaks were weak [Fig. 2(c)]. The spin excitation also disappeared at 7 K.

Nuclear structure of BCNS at a uniaxial pressure of 1 MPa at 200 K upon cooling was analyzed. The integrated intensities of 20 reflections were refined with an orthorhombic space group ( $Cmme$ , No. 67) with lattice parameters  $a = b = 6.43$  Å and  $c = 8.91$  Å. Observed nuclear Bragg peak intensities are shown in Fig. 3 as a function of calculated intensity. The refined crystallographic parameters are listed in Table I. The nuclear structure parameters are almost consistent with the reported values [30].

Magnetic structures were analyzed at uniaxial pressures of 0.1 and 1 MPa. Although it was a tetragonal state, the analyses were performed as an orthorhombic state due to magnetically broken  $C_4$  symmetry. For the magnetic structure analysis, integrated intensities of 16 reflections were refined with twin models, where the isotropic magnetic form factors of  $\text{Co}^{2+}$  and  $\text{Ni}^{2+}$  were used. In the previous analysis, the magnetic moments of BCNS were found to align within the (Co,Ni)S plane [14], where the magnetic moment direction in the plane could not be determined due to the degeneracy in the tetragonal state. Based on the result, the following four types of magnetic structures are considered: two types of magnetic wave vectors,  $\mathbf{Q}_1$  ( $\mathbf{k} = [1, 0, 0]$ ) and  $\mathbf{Q}_2$  ( $\mathbf{k} = [0, 1, 0]$ ), and two spin directions,  $m//a$  and  $m//b$ . After these refinements, the possible spin rotation in the plane was checked. Two of these four magnetic structures form a twin, leading to two twin models. The first twin model consists of two magnetic domains of  $\mathbf{Q}_1$  with  $m//a$  and  $\mathbf{Q}_2$  with  $m//b$ . The second twin

TABLE I. Crystallographic parameters and conventional reliability factors ( $R$  factors) obtained from the structural refinement of BCNS, with a space group of  $Cmme$ , No. 67 at a uniaxial pressure of 1 MPa. Standard deviations are shown in the parentheses at the corresponding digit.

Element	Site	$x$	$y$	$z$	$B_{iso}(\text{fix})$	$g(\text{fix})$
Ba	4g	0.000	0.250	0.798(3)	0.500	1.00
Co	4g	0.000	0.250	0.399(7)	0.500	0.90
Ni	4g	0.000	0.250	0.399(7)	0.500	0.10
$S_1$	4g	0.000	0.250	0.161(7)	0.500	0.88
$S_2$	4b	0.250	0.000	0.500	0.500	1.00

Nuclear reflections:  $R_{F2} = 11.5\%$  and  $R_F = 5.61\%$

model consists of two magnetic domains of  $\mathbf{Q}_1$  with  $m//b$  and  $\mathbf{Q}_2$  with  $m//a$ . The only difference between these twin models is the spin direction.

At 0.1 MPa, integrated intensities of 16 reflections at 240 K upon warming were refined with the orthorhombic twin models. Those refined results are shown in Figs. 4(a) and 4(b), where the twin ratios are also refined. The second model in

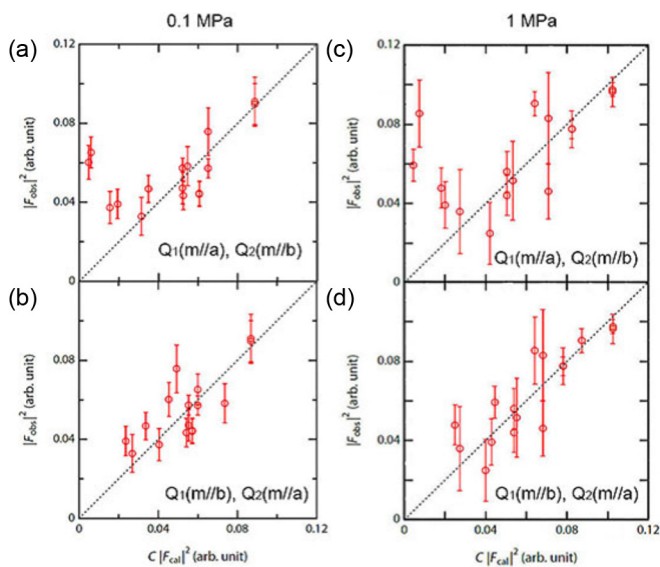


FIG. 4. Observed magnetic Bragg peak intensities at uniaxial pressures of 0.1 and 1 MPa as a function of calculated intensity upon cooling. (a) A twin model of two magnetic structures of  $\mathbf{Q}_1$  with  $m//a$  and  $\mathbf{Q}_2$  with  $m//b$  at 0.1 MPa. The twin ratio of these was refined as 0.44(10) to 0.56(10), respectively. The magnetic moment per  $\text{Co}_{0.9}\text{Ni}_{0.1}$  was  $2.14 \pm 0.13 \mu_B$ . The conventional reliability factor  $R_F$  was 18.3%. (b) A twin model of two magnetic structures of  $\mathbf{Q}_1$  with  $m//b$  and  $\mathbf{Q}_2$  with  $m//a$  at 0.1 MPa. The twin ratio of these was refined as 0.48(5) to 0.52(5), respectively. The magnetic moment per  $\text{Co}_{0.9}\text{Ni}_{0.1}$  was  $2.13 \pm 0.06 \mu_B$ . The conventional reliability factor  $R_F$  was 9.38%. (c) A twin model of two magnetic structures of  $\mathbf{Q}_1$  with  $m//a$  and  $\mathbf{Q}_2$  with  $m//b$  at 1 MPa. The twin ratio of these was refined as 0.38(10) to 0.62(10), respectively. The magnetic moment per  $\text{Co}_{0.9}\text{Ni}_{0.1}$  was  $2.34 \pm 0.15 \mu_B$ . The conventional reliability factor  $R_F$  was 19.7%. (d) A twin model of two magnetic structures of  $\mathbf{Q}_1$  with  $m//b$  and  $\mathbf{Q}_2$  with  $m//a$  at 1 MPa. The twin ratio of these was refined as 0.41(4) to 0.59(4), respectively. The magnetic moment per  $\text{Co}_{0.9}\text{Ni}_{0.1}$  was  $2.33 \pm 0.06 \mu_B$ . The conventional reliability factor  $R_F$  was 8.54%.

Fig. 4(b) is much better than the first one in Fig. 4(a). The small  $R_F$  value of 9.38% confirms nearly equal ratio  $52 \pm 5\%$  of a magnetic domain of  $\mathbf{Q}_2$  with  $m//a$  to the other of  $\mathbf{Q}_1$  with  $m//b$ . At 1 MPa, integrated intensities of 16 reflections at 200 K upon cooling were refined with the orthorhombic twin models. Those refined results are shown in Figs. 4(c) and 4(d). The second model in Fig. 4(d) is much better than the first one in Fig. 4(c) again. This result shows that the magnetic domain of  $\mathbf{Q}_2$  with  $m//a$  increases from  $52 \pm 5\%$  to  $59 \pm 4\%$  with increasing the uniaxial pressure. The magnetic moment direction may rotate from the  $a$  axis to some extent. Possible spin rotations in the plane were checked by using the twin models. For example, a positive  $\pi/6$  spin rotation (anticlockwise) resulted in 25.0% of  $R_F$ , whereas a negative  $\pi/6$  spin rotation (clockwise) resulted in 29.8% of  $R_F$ . These much worse  $R_F$  values than 8.54% confirm that the magnetic moments preferentially align around the  $a$  axis in the major domain of  $\mathbf{Q}_2$ .

Although the integrated intensities are scattered with large error bars in Fig. 4, the clear difference between the two twin models is obvious especially at the low calculated intensities. The reason for data scattering may be attributed to the coarse rotation step in the crystal measurement and the isotropic magnetic form factors used in the analyses. The peak intensities near the detector edges were removed due to the uncertainty. The neutron absorption effect in the aluminum folder was neglected in these analyses.

The domain ratio change by the uniaxial pressure supports that the orbital degeneracy of  $zx$  and  $yz$  orbitals is lifted even in this AFI phase, leading to the modification of exchange couplings. The obtained nuclear structure with the main magnetic structure at the uniaxial pressure is shown in Fig. 1(c). Note that the dominant magnetic wave vector in both two twin models was  $\mathbf{Q}_2$ , corresponding to the observed anisotropic inelastic neutron scattering pattern, regardless of the spin directions.

The structural phase transition of BCNS takes place from tetragonal to orthorhombic phases in the temperature range from 185 to 235 K. Accordingly, orthorhombic 400 Bragg peak splits into two peaks. When the peaks are fitted by two Gaussian peaks, the two peak heights become a good measure of the transition. Figure 5 shows the temperature dependence of the two peak heights at 400 and 040 under uniaxial pressures  $P = 0.1$  and 1 MPa upon cooling. The transition temperatures increased by 2.8(9) K and 3.8(9) K with increasing the uniaxial pressure for the original peak in

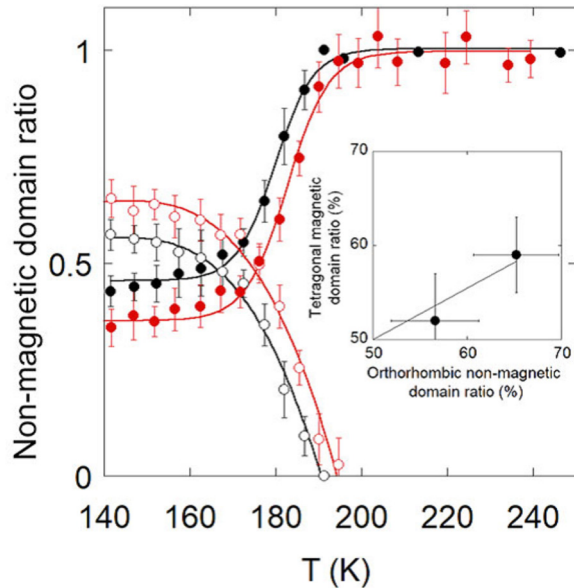


FIG. 5. Temperature dependence of nonmagnetic domain ratio under uniaxial pressures  $P = 0.1$  (black open and closed circles) and 1 MPa (red open and closed circles). The temperature dependences are fitted by a tanh function and a cubic polynomial to estimate the transition temperatures. The transition temperature increased at 1 MPa from that of 0.1 MPa. Inset shows the observed relationship between the orthorhombic nonmagnetic domain ratio and the tetragonal magnetic domain ratio of  $\mathbf{Q}_2$  with  $m//a$  at the same uniaxial pressure.

the tetragonal phase and the new peak in the orthorhombic phase, respectively. This increasing shift is opposite to the decreasing shift of transition temperature measured at uniform pressure [18]. These nonmagnetic domain ratios in the orthorhombic phase were  $56.6 \pm 4.6\%$  and  $65.2 \pm 4.5\%$  in the whole volume at  $T = 140$  K for 0.1 and 1 MPa, respectively (Fig. 5). However, according to the magnetic structure analysis, the magnetic domain ratios of  $\mathbf{Q}_2$  with  $m//a$  in the tetragonal phase were  $52 \pm 5\%$  and  $59 \pm 4\%$  at the uniaxial pressures of 0.1 and 1 MPa, respectively. These magnetic domain ratios are surprisingly similar to the nonmagnetic domain ratios in the orthorhombic phase, although the tetragonal values are slightly smaller than the orthorhombic values as shown in the inset of Fig. 5.

### B. Magnetic excitation under a uniaxial pressure

Magnetic excitation spectrum was measured at  $T = 200$  K upon cooling under a uniaxial pressure of 1 MPa. Figure 6 shows constant-energy cuts of dynamical structure factor  $S(\mathbf{Q}, E)$  along  $H$  and  $K$ . The vertically integrated width is  $\pm 0.3$  r.l.u. Figure 7 shows constant- $Q$  cuts of  $S(\mathbf{Q}, E)$  at zone boundaries. Although the data are scattered in Fig. 7, three peaks are expected in the twin model based on the spin-wave calculation. The first one is the lowest-energy peak at 53 meV in Fig. 7(a). The second one is the middle-energy peak at about 59 meV in all the three figures in Figs. 7(a), 7(b) and 7(c). The last one is the highest-energy peak at about 70 meV in Figs. 7(b) and 7(c). Note that these peak energies observed

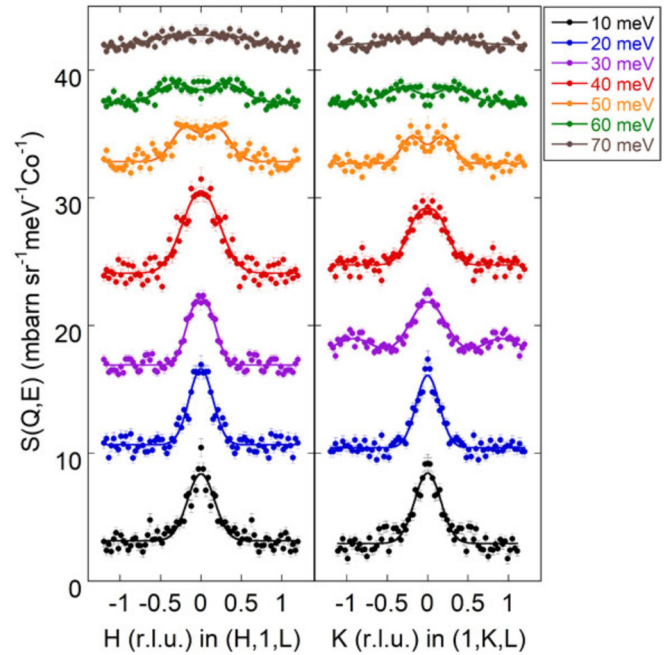


FIG. 6. Constant-energy cuts of dynamical structure factor  $S(\mathbf{Q}, E)$  along  $H$  and  $K$  at a uniaxial pressure of 1 MPa. Two equivalent data sets in the  $(H, K)$  plane were averaged and symmetrized, based on the  $C_2$  symmetry. The intensities are integrated in  $\pm 0.3$  r.l.u. along the normal direction to the corresponding scan direction of  $H$  or  $K$ .  $E_i$  is 54.1 meV for  $E = 10, 20,$  and  $30$  meV, whereas  $E_i$  is 120.0 meV for the other energies above 30 meV.

at constant- $Q$  scan are smoothly connected to the dispersions observed by constant- $E$  scans.

The  $L$ -dependence of inelastic scattering intensity is shown in Fig. 8, where the transfer energy also increases with increasing  $L$  due to the scattering geometry of a single scan. The continuous intensity along  $L$  direction in Fig. 8(b) suggests that the spin-wave dispersion is lower than the energy in Fig. 8(a). As for the other reciprocal directions in Fig. 8(b), the dispersion sharply increases like a chimney in this low energy range. Based on the magnetic structure in Fig. 1, the exchange interaction between the equivalent sites along the  $c$  axis,  $J_c$ , is ferromagnetic. Therefore, the spin-wave dispersion along  $L$  is expected to be a sine function, increasing from  $L = 0$  and becoming maximum at  $L = 0.5$ . Then, we can conclude that the gap energy is less than 2 meV at  $L = 0$ . The maximum energy is below 5 meV at  $(0, -1, 0.5)$ .

Because of the small gap below 2 meV at  $L = 0$ , the four exchange parameters multiplied by  $S$ ,  $SJ_{1a}$ ,  $SJ_{1b}$ ,  $SJ_2$ , and  $SJ_c$  [Fig. 1(a)], are considered in the spin-wave model without a gap. Based on the magnetic structure in Fig. 1(c), the exchange interaction between the equivalent sites along the  $c$ -axis,  $J_c$ , is ferromagnetic. The maximum energy at  $L = 0.5$  leads to a lower limit of  $-0.06$  meV on  $SJ_c$  based on our spin-wave calculation. The highest energy at  $(1, 0.5)$  reaches about 70 meV. Based on the high zone-boundary energies in Fig. 7, the exchange parameters of  $S(J_{1a} + J_{1b})/2$  and  $SJ_2$  were estimated as  $-3.5$  and  $14.0$  meV, respectively.  $SJ_2$  determines the average energy scale of the spin-wave dispersions, whereas  $S(J_{1a} + J_{1b})/2$  corresponds to the splitting energies

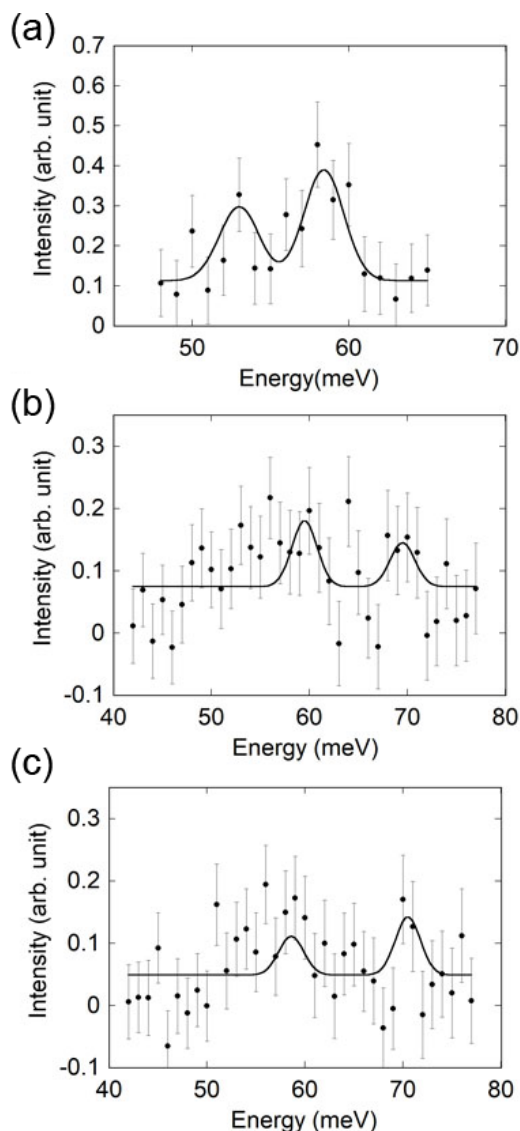


FIG. 7. Constant- $Q$  cuts of dynamical structure factor multiplied by  $E$ ,  $S(\mathbf{Q}, E) \times E$ , at zone boundaries at a uniaxial pressure of 1 MPa. Intensities were subtracted by those at  $(1, 1)$  as background. (a) Zone boundary energies at  $(0.5, 0)$  were estimated as  $53.0 \pm 0.7$  and  $58.4 \pm 0.3$  meV from the fit with a fixed full-width at half maximum of 3 meV. (b) Zone boundary energies at  $(0.5, 1)$  were  $59.5 \pm 0.8$ , and  $69.5 \pm 1.1$  meV. (c) Zone boundary energies at  $(1, 0.5)$  were  $58.6 \pm 0.5$ , and  $70.5 \pm 1.4$  meV. Because of the twin model with  $C_2$  symmetry, these peak energies at  $(1, 0.5)$  are expected to be the same as those at  $(0.5, 1)$ . Based on these energies, basic spin-wave parameters  $S(J_{1a} + J_{1b})/2$  and  $SJ_2$  were determined. The solid lines are guides to the eye with expected intensity ratio from the spin-wave calculation.

of the branches at the zone boundaries in Fig. 7. The in-plane anisotropy of  $SJ_1$  was sensitive to the energy gap of about 25 meV at  $(1, 0)$ . Without  $SJ_1$ , the in-plane excitation becomes isotropic.

The estimated exchange parameters are  $SJ_{1a} = -4.3 \pm 0.5$  meV,  $SJ_{1b} = -2.7 \pm 0.5$  meV,  $SJ_2 = 14.0 \pm 0.5$  meV, and  $0 \geq SJ_c \geq -0.06$  meV. The errors correspond to the uncertainty of the peak positions in Fig. 7. The

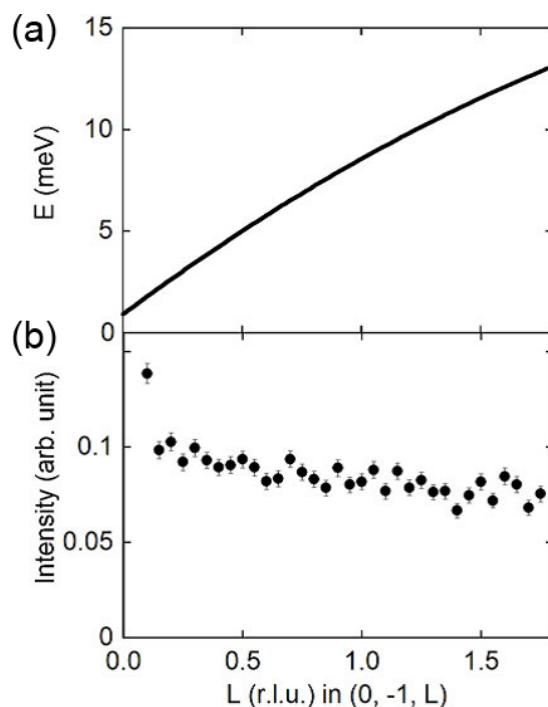


FIG. 8.  $L$ -dependence of magnetic excitation with an incident energy of 19.7 meV at a uniaxial pressure of 1 MPa. (a) In this measurement configuration,  $E$  increases from 0 to 8 meV with increasing  $L$  from 0 to 1 r.l.u. (b) The intensity was integrated in the reciprocal region of  $(H, K) = (0 \pm 0.2, -1 \pm 0.2)$ . The continuous intensity along  $L$  suggests that the two-dimensional nature of a magnetic rod in this energy range.

out-of-plane anisotropy ratio of  $J_2/|J_c|$  reaches 240. This strong two-dimensionality of the magnet is consistent with a magnetic rod observed in our previous measurement on  $\text{BaCo}_{0.82}\text{Ni}_{0.18}\text{S}_2$  [14]. Thus, the magnetic interactions in this layered material are essentially two-dimensional.

Figures 9(a)–9(c) show the constant-energy cuts of the observed dynamical structure factor,  $S(\mathbf{Q}, E)$ , in the  $(H, K)$  plane at three transfer energies ( $E = 40, 50$ , and 60 meV). The in-plane anisotropy emerges with increasing energy. Figures 9(d)–9(f) show the constant-energy cuts of the simulated spin excitations at the corresponding energies to Figs. 9(a)–9(c), reproducing the anisotropy growing along with the transferred energy. Figure 10 shows the observed (closed circles) and calculated spin-wave dispersions.

The momentum-integrated dynamical spin susceptibilities  $\chi''(E)$  at two different reciprocal regions of  $(H, 1)$  and  $(1, K)$  are shown as a function of energy in Fig. 11. The absolute value is estimated based on the anisotropic paramagnetic susceptibility model [27]. The integrated region is 60% of one Brillouin zone. Within the region, the integrated dynamical spin susceptibility results in about  $11.1 \pm 0.6 \mu_B^2$  from Fig. 11. Fully integrated dynamical spin susceptibility in  $Q$  and  $E$  becomes  $g^2S(S+1)$ . According to our magnetic structure analysis, the magnetic moment was  $2.33 \pm 0.06 \mu_B$  at  $T = 200$  K. This value is fairly consistent with the integrated intensity. Note that the overlapping region at  $(1, 1)$  in the two scans along  $(H, 1)$  and  $(1, K)$  does not have any

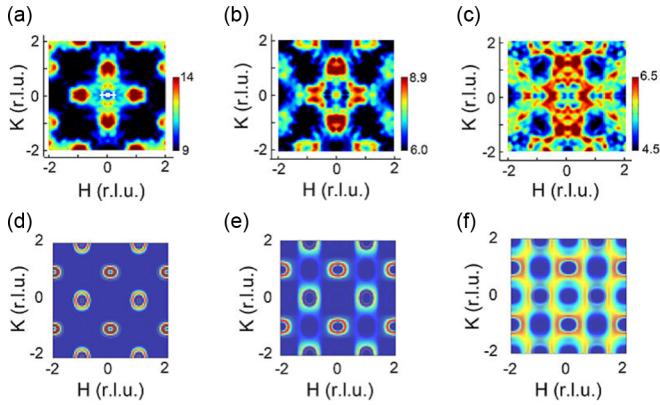


FIG. 9. Constant-energy slices of dynamical structure factor  $S(\mathbf{Q}, E)$  in the  $(H, K)$  plane at a uniaxial pressure of 1 MPa. (a–c)  $S(\mathbf{Q}, E)$  in the  $(H, K)$  plane at  $E = 40$  (a), 50 (b), and 60 (c) meV. Each slice is integrated in the energy width of 10 meV. The incident energy is  $E_i = 120.0$  meV. The color bars are in units of  $\text{mbar sr}^{-1} \text{meV}^{-1} \text{Co}^{-1}$ . The quadrant intensity is averaged based on the  $C_2$  symmetry. (d–f) Theoretical simulations of a twin model with a ratio of 60:40 at  $E = 40$  (d), 50 (e), and 60 (f) meV for  $|H| \leq 2$  and  $|K| \leq 2$  r.l.u. The used exchange coupling parameters are  $SJ_{1a} = -4.3$  meV,  $SJ_{1b} = -2.7$  meV,  $SJ_2 = 14.0$  meV, and  $SJ_c = -0.06$  meV.

significant intensity in this magnet. The calculated dynamical spin susceptibility in Fig. 11 is based on a twin model with the twin ratio of 60 to 40, where the total intensity was adjusted arbitrarily. As for the calculated energy dependence, the  $\chi''(E)$  sharply increases from 25 meV corresponding to the appearance of a new branch with increasing energy. In addition, at  $E = 60$  meV, the large intensity difference between  $(H, 1)$  and  $(1, K)$  appears in the twin model. The anisotropy at 60 meV is consistent with the intensity anisotropy observed in Fig. 9(c).

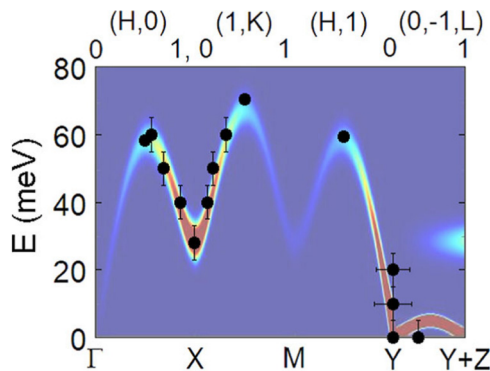


FIG. 10. Observed dispersion (filled circles) and calculated spin-wave dispersion with  $SJ_{1a} = -4.3$  meV,  $SJ_{1b} = -2.7$  meV,  $SJ_2 = 14.0$  meV, and  $SJ_c = -0.06$  meV. The maximum energy of the dispersion from Y to Y+Z points is limited below 5 meV. Because of the quasi-two-dimensionality,  $L$  is neglected for the other spectra. The calculated dispersions are drawn with a full-width at half-maximum of 8 meV, except for the dispersion along  $L$  in  $(0, -1, L)$ , where the width is 2 meV to show the low energy dispersion.

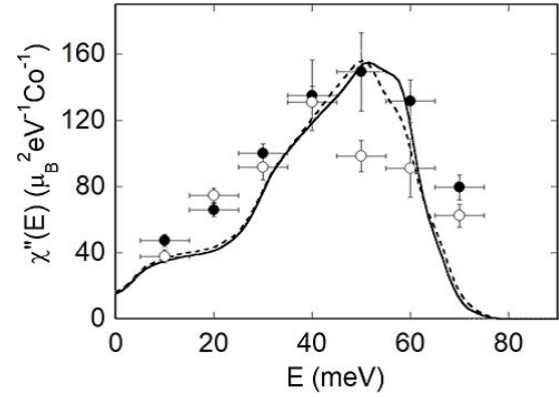


FIG. 11. Momentum-integrated dynamical spin susceptibility  $\chi''(E)$  at a uniaxial pressure of 1 MPa. The closed circles are integrated along  $H$  in  $(H, 1)$  within  $|K - 1| \leq 0.3$  r.l.u. of  $\chi''(\mathbf{Q}, E)$  at 200 K on cooling. The open circles are along  $K$  in  $(1, K)$  within  $|H - 1| \leq 0.3$  r.l.u. The solid and dashed lines were calculated dynamical spin susceptibilities of the twin model integrated along  $H$  in  $(H, 1)$  and  $K$  in  $(1, K)$ , respectively. They were calculated based on the spin-wave model with a twin ratio of 60:40. The used exchange parameters were  $SJ_{1a} = -4.3$  meV,  $SJ_{1b} = -2.7$  meV,  $SJ_2 = 14.0$  meV, and  $SJ_c = -0.06$  meV. The horizontal error bar is the integrated region in energy.

#### IV. DISCUSSION

So far, AF stripe orders are always accompanied with orthorhombic distortion in the lattice [3,5,6,10], suggesting the strong coupling between them. In contrast to these previous materials, the present AF stripe order takes place in the tetragonal state without any strain, suggesting the weak coupling. Nevertheless, the magnetic domain ratio was changed by weak uniaxial pressures, while the lattice keeps the tetragonal symmetry within our experimental accuracy. Here, lifting the degeneracy by a strain enables us to solve the magnetic structure. The static magnetic structure and the inelastic neutron scattering spectrum exhibit mutually consistent result of the dominant spin configuration of  $\mathbf{Q}_2$  [Fig. 1(b)].

Within the calculation without a magnetic anisotropy term by SPINW, there was no energy difference between  $\mathbf{Q}_1$  and  $\mathbf{Q}_2$  stripe orders in the tetragonal lattice. This degeneracy of these two stripe orders corresponds to the coexistence of  $\mathbf{Q}_1$  and  $\mathbf{Q}_2$  domains, suggesting the stripe order fluctuation as the domain fluctuation. It can also be interpreted as the spin nematic fluctuation above the Néel temperature. By applying an in-plane uniaxial pressure, one domain with  $\mathbf{Q}_2$  was preferred. This feature is common with the case of iron-based materials [11,12]. It suggests that the orbital degeneracy is lifted in the electronic state. In our previous magnetic form factor analysis [14], two sets of  $\{(x^2 - y^2), (3z^2 - r^2), \text{and } ((yz + zx)/2)\}$  and  $\{(x^2 - y^2), (3z^2 - r^2), \text{and } xy\}$  approximately reproduced the observed magnetic Bragg peak intensities. Here, the former set has the orbital degeneracy of  $yz$  and  $zx$  corresponding to the present in-plane broken symmetry by a uniaxial pressure. Based on this result, we conclude that the electron configuration  $3d^{7+x+2y}$  of BCNS consists of  $x^2 - y^2$ ,  $3z^2 - r^2$ ,  $yz$ , and  $zx$  unpaired electrons in the pyramidal coordination of  $\text{Co}(\text{Ni})^{2+}$ . The present result is consistent with

recent electronic structure calculations, where the unpaired electrons of  $\text{Co}^{2+}$  sit on  $x^2 - y^2$ ,  $yz$ , and  $zx$  orbitals whereas those of  $\text{Ni}^{2+}$  are on  $x^2 - y^2$  and  $3z^2 - r^2$  [31,32]. The electronic state with the orbital degeneracies of  $yz$  and  $zx$  unpaired electrons is the same as those observed in iron-based parent materials [3], where only  $yz$  and  $zx$  are predominantly unpaired in the tetrahedral coordination of  $\text{Fe}^{2+}$  with  $3d^6$ . Therefore, we may expect the lifting of orbital degeneracy in this system. However, because the AF stripe order in this BCNS takes place in the tetragonal insulating state, the orbital mechanism with itinerant electrons [33–35] cannot be the primary origin. The remaining possible mechanism is a magnetic scenario with in-plane symmetry breaking in the spin-spin correlations of AF stripe order [1,36,37]. The present result supports the magnetic scenario for this insulating BCNS. Two magnetic domains with  $\mathbf{Q}_1$  and  $\mathbf{Q}_2$  AF stripe orders coexist, where domains can be inherently fluctuating in the tetragonal state like an iron-based compound [10]. The fluctuating frequency could be estimated from quasielastic scattering at low-energies. In our magnetic structure analysis, the magnetic inelastic scattering signals are integrated in an energy range from  $-10$  meV to  $10$  meV, suggesting the typical frequency below a few THz.

Strong uniform pressure effect [18] can also be explained by the electron configuration. The uniform pressure is expected to lift the  $x^2 - y^2$  orbital energy, leading to the electron transfer from the  $x^2 - y^2$  orbital to  $zx$  and  $yz$  orbitals. It effectively dopes electrons in  $zx$  and  $yz$  orbitals.

Note that the AFI phase of BCNS locates at higher temperatures than the PM phase in contrast to the other MI transition

materials such as  $\text{V}_2\text{O}_3$  [38]. This is very unusual suggesting that the high-temperature insulator phase of BCNS might be stabilized by the present stripe order fluctuation. This is an intriguing subject to study their relationship in the future.

## V. SUMMARY

We revealed magnetic in-plane broken  $C_4$  symmetry of BCNS in the tetragonal state under weak uniaxial strains by neutron scattering. By applying the strain, the hidden magnetic structure of BCNS was revealed. The magnetic domain ratio in the tetragonal state is only slightly smaller than the nonmagnetic domain ratio in the orthorhombic lattice. Based on our spin-wave calculation, this novel stripe order excitation is quantitatively reproduced by in-plane anisotropic  $J_{1a} - J_{1b} - J_2$  model. The present dataset represents essential features of the full momentum dispersion of the in-plane anisotropic magnetic excitations of this novel AF stripe order in the tetragonal state.

## ACKNOWLEDGMENTS

This work at J-PARC has been performed at 4SEASONS(BL01) under Proposals No. 2019A0290 and No. 2019I0001. We thank Drs. K. Kodama, H. Onishi, K. Shibata, Qi Sheng, H. Harashina, and K. Yamamoto, and Profs. A. Gauzzi, Y. J. Uemura, C. Q. Jin, and L.-J. Chang for discussions, and Mr. M. Usami in JAEA technical support team for making the uniaxial pressure device. J.I. acknowledges the financial support of Houga Kenkyu in JAEA.

- 
- [1] R. M. Fernandes and J. Schmalian, Manifestations of nematic degrees of freedom in the magnetic, elastic, and superconducting properties of the iron pnictides, *Supercond. Sci. Technol.* **25**, 084005 (2012).
- [2] R. M. Fernandes, A. V. Chubukov, and J. Schmalian, What drives nematic order in iron-based superconductors? *Nat. Phys.* **10**, 97 (2014).
- [3] P. Dai, Antiferromagnetic order and spin dynamics in iron-based superconductors, *Rev. Mod. Phys.* **87**, 855 (2015).
- [4] J. Sudan, A. Lüscher, and A. M. Läuchli, Emergent multipolar spin correlations in a fluctuating spiral: The frustrated ferromagnetic spin-1/2 Heisenberg chain in a magnetic field, *Phys. Rev. B* **80**, 140402(R) (2009).
- [5] Y. Song, H. Cao, B. C. Chakoumakos, Y. Zhao, A. Wang, H. Lei, C. Petrovic, and R. J. Birgeneau, Intertwined Magnetic and Nematic Orders in Semiconducting  $\text{KFe}_{0.8}\text{Ag}_{1.2}\text{Te}_2$ , *Phys. Rev. Lett.* **122**, 087201 (2019).
- [6] Y. D. Song, X. Lu, E. Bourret-Courchesne, and R. J. Birgeneau, Strain-Induced Spin-Nematic State and Nematic Susceptibility Arising from  $2 \times 2$  Fe Clusters in  $\text{KFe}_{0.8}\text{Ag}_{1.2}\text{Te}_2$ , *Phys. Rev. Lett.* **123**, 247205 (2019).
- [7] J. H. She, M. J. Lawler, and E.-A. Kim, Quantum Spin Liquid Intertwining Nematic and Superconducting Order in FeSe, *Phys. Rev. Lett.* **121**, 237002 (2018).
- [8] H.-H. Lai, W.-J. Hu, E. M. Nica, R. Yu, and Q. Si, Antiferroquadrupolar Order and Rotational Symmetry Breaking in a Generalized Bilinear-Biquadratic Model on a Square Lattice, *Phys. Rev. Lett.* **118**, 176401 (2017).
- [9] Jun Zhao *et al.*, Spin waves and magnetic exchange interactions in  $\text{CaFe}_2\text{As}_2$ , *Nat. Phys.* **5**, 555 (2009).
- [10] C. Dhital, Z. Yamani, W. Tian, J. Zeretsky, A. S. Sefat, Z. Wang, R. J. Birgeneau, and S. D. Wilson, Effect of Uniaxial Strain on the Structural and Magnetic Phase Transitions in  $\text{BaFe}_2\text{As}_2$ , *Phys. Rev. Lett.* **108**, 087001 (2012).
- [11] Xingye Lu *et al.*, Spin Waves in Detwinned  $\text{BaFe}_2\text{As}_2$ , *Phys. Rev. Lett.* **121**, 067002 (2018).
- [12] Xingye Lu *et al.*, Nematic spin correlations in the tetragonal state of uniaxial-strained  $\text{BaFe}_{2-x}\text{Ni}_x\text{As}_2$ , *Science* **345**, 657 (2014).
- [13] Chen Tong *et al.*, Anisotropic spin fluctuations in detwinned FeSe, *Nature Mater.* **18**, 709 (2019).
- [14] S. Shamoto, K. Kodama, H. Harashina, M. Sato, and K. Kakurai, Neutron scattering study of  $\text{BaCo}_{0.82}\text{Ni}_{0.18}\text{S}_2$ , *J. Phys. Soc. Jpn.* **66**, 1138 (1997).
- [15] L. S. Martinson, J. W. Schweitzer, and N. C. Baenziger, Metal-Insulator Transitions in  $\text{BaCo}_{1-x}\text{Ni}_x\text{S}_{2-y}$ , *Phys. Rev. Lett.* **71**, 125 (1993).
- [16] Z. Guguchia, B. A. Frandsen, D. Santos-Cottin, S. C. Cheung, Z. Gong, Q. Sheng, K. Yamakawa, A. M. Hallas, M. N. Wilson, Y. Cai, J. Beare, R. Khasanov, R. DeRenzi, G. M. Luke, S. Shamoto, A. Gauzzi, Y. Klein, and Y. J. Uemura, Probing the quantum phase transition in Mott insulator  $\text{BaCoS}_2$  tuned by



- pressure and Ni substitution, *Phys. Rev. Materials* **3**, 045001 (2019).
- [17] T. Sato, H. Kumigashira, D. Ionel, T. Takahashi, I. Hase, H. Ding, J. C. Campuzano, and S. Shamoto, Evolution of metallic states from the Hubbard band in the two-dimensional Mott system  $\text{BaCo}_{1-x}\text{Ni}_x\text{S}_2$ , *Phys. Rev. B* **64**, 075103 (2001).
- [18] C. Looney, J. S. Schilling, L. S. Martinson, and J. W. Schweitzer, Influence of Hydrostatic Pressure on the Insulator-Metal Transition in  $\text{BaCo}_{0.9}\text{Ni}_{0.1}\text{S}_{1.9}$ , *Phys. Rev. Lett.* **76**, 4789 (1996).
- [19] B. Fisher *et al.*, Metal-insulator transition upon heating and negative-differential-resistive-switching induced by self-heating in  $\text{BaCo}_{0.9}\text{Ni}_{0.1}\text{S}_{1.8}$ , *Appl. Phys. Lett.* **104**, 153511 (2014).
- [20] S. A. M. Mentink, T. E. Mason, B. Fisher, J. Genossar, L. Patlagan, A. Kanigel, M. D. Lumsden, and B. D. Gaulin, Antiferromagnetism, structural properties, and electronic transport of  $\text{BaCo}_{0.9}\text{Ni}_{0.1}\text{S}_{1.8}$ , *Phys. Rev. B* **55**, 12375 (1997).
- [21] S. Shamoto, S. Tanaka, E. Ueda, and M. Sato, Single crystal growth of  $\text{BaNiS}_2$ , *J. Cryst. Growth* **154**, 197 (1995).
- [22] R. Kajimoto *et al.*, The Fermi chopper spectrometer 4SEASONS at J-PARC, *J. Phys. Soc. Jpn.* **80**, SB025 (2011).
- [23] M. Nakamura, R. Kajimoto, Y. Inamura, F. Mizuno, M. Fujita, T. Yokoo, and M. Arai, First demonstration of novel method for inelastic neutron scattering measurement utilizing multiple incident energies, *J. Phys. Soc. Jpn.* **78**, 093002 (2009).
- [24] J. Rodriguez-Carvajal, Recent advances in magnetic structure determination by neutron powder diffraction + FullProf, *Physica B (Amsterdam, Neth.)* **192**, 55 (1993).
- [25] K. Momma, and F. Izumi, VESTA: a three-dimensional visualization system for electronic and structural analysis, *J. Appl. Crystallogr.* **41**, 653 (2008).
- [26] Y. Inamura, T. Nakatani, J. Suzuki, and T. Otomo, Development status of software “Utsusemi” for chopper spectrometers at MLF, J-PARC, *J. Phys. Soc. Jpn.* **82**, SA031 (2013).
- [27] C. Lester, J.-H. Chu, J. G. Analytis, T. G. Perring, I. R. Fisher, and S. M. Hayden, Dispersive spin fluctuations in the nearly optimally doped superconductor  $\text{Ba}(\text{Fe}_{1-x}\text{Co}_x)_2\text{As}_2$  ( $x = 0.065$ ), *Phys. Rev. B* **81**, 064505 (2010).
- [28] S. Toth and B. Lake, Linear spin wave theory for single- $Q$  incommensurate magnetic structures, *J. Phys.: Condens. Matter* **27**, 166002 (2015).
- [29] R. A. Ewings, A. Buts, M. D. Lee, J. van Duijn, I. Bustinduy, T. G. Perring, Horace: Software for the analysis of data from single crystal spectroscopy experiments at time-of-flight neutron instruments, *Nucl. Instrum. Methods Phys. Res. Sect. A* **834**, 132 (2016).
- [30] K. Kodama, S. Shamoto, H. Harashina, J. Takeda, M. Sato, K. Kakurai, and M. Nishi, Electronic structure of the quasi-two-dimensional Mott system  $\text{BaCo}_{1-x}\text{Ni}_x\text{S}_2$ , *J. Phys. Soc. Jpn.* **65**, 1782 (1996).
- [31] D. Santos-Cottin *et al.*, Rashba coupling amplification by a staggered crystal field, *Nat. Commun.* **7**, 11258 (2016).
- [32] N. Nilforoushan *et al.*, Tuning Dirac nodes with correlated d-electrons in  $\text{BaNiS}_2$ , [arXiv:1905.12210](https://arxiv.org/abs/1905.12210).
- [33] W. Lv, J. Wu, and W. Ku, Orbital ordering induces structural phase transition and the resistivity anomaly in iron pnictides, *Phys. Rev. B* **80**, 224506 (2009).
- [34] C.-C. Lee, W.-G. Yin, and W. Ku, Ferro-Orbital Order and Strong Magnetic Anisotropy in the Parent Compounds of Iron-Pnictide Superconductors, *Phys. Rev. Lett.* **103**, 267001 (2009).
- [35] S. Liang, A. Moreo, and E. Dagotto, Nematic State of Pnictides Stabilized by Interplay Between Spin, Orbital, and Lattice Degrees of Freedom, *Phys. Rev. Lett.* **111**, 047004 (2013).
- [36] C. Fang, H. Yao, W.-F. Tsai, J. Hu, and S. A. Kivelson, Theory of electron nematic order in  $\text{LaFeAsO}$ , *Phys. Rev. B* **77**, 224509 (2008).
- [37] C. Xu, M. Müller, and S. Sachdev, Ising and spin orders in the iron-based superconductors, *Phys. Rev. B* **78**, 020501(R) (2008).
- [38] B. A. Frandsen *et al.*, Volume-wise destruction of the antiferromagnetic Mott insulating state through quantum tuning, *Nat. Commun.* **7**, 12519 (2016).